Numerical investigation of the influence of defects on the multiaxial fatigue strength of additively manufactured alloys

Sai Sreeniva Penkulinti, Matthieu Bonneric, Nicolas Saintier, Benoit Verquin, Fabien Lefebvre, Thierry Palin-Luc, Pascal Ghys

Available online at www.sciencedirect.com

ScienceDirect

Procedia Structural Integrity 57 (2024) 824–832

Structural Integrity Procedia

www.elsevier.com/locate/procedia

Fatigue Design 2023 (FatDes 2023)

Numerical investigation of the influence of defects on the multiaxial fatigue strength of additively manufactured alloys

Sai Sreenivas PENKULINTI[a,*], Matthieu BONNERIC[a], Nicolas SAINTIER[a], Benoit VERQUIN[b], Fabien LEFEBVRE[c], Thierry PALIN-LUC[a], Pascal GHYS[d]

[a] *I2M, Arts et métiers ParisTech - CNRS UMR 5295, Université de Bordeaux, Talence, France*
[b] *CETIM, 7 rue de la presse, Saint-Etienne, France*
[c] *CETIM, 52 avenue Félix Louat, Senlis, France*
[d] *ALSTOM, 48 Rue Albert Dhalenne, Saint-Ouen-sur-Seine, France*

Abstract

Laser Powder Bed Fusion (L-PBF) is one of the Additive Manufacturing (AM) techniques that have revealed salient advantages in enabling the fabrication of 3D parts with intricate shapes and added functionalities. Despite many advances, scientific challenges still exist. One of them, especially where the additively manufactured industrial components undergo fatigue loading, is the defects (gas pores and Lack of Fusions (LoFs)) that are induced during the fabrication process. The present work aims to investigate the influence of AM defects on fatigue strength under multiaxial loading conditions. From numerical simulations, the key question addressed is the impact of defects' morphology on their criticality under multiaxial loadings. Finite Element (FE) elastic simulations at load ratio $R = -1$ under multiaxial loading conditions (tension, torsion and tension-torsion) have been performed on numerically generated spherical defect and LoFs obtained from micro-CT scans of additively manufactured TA64 alloy. The Crossland criterion (stress-based) was used to evaluate the fatigue strength and the obtained numerical results were compared with the available experimental results.

Keywords: Additive Manufacturing; Defect; Multiaxial fatigue; Finite Element Analysis; Crossland criterion.

1. Introduction

Aside from the ability to make metal components out of a variety of alloys, the current success of the Laser Powder Bed Fusion (L-PBF) technique can be attributed to the following factors: the ability to optimise the microstructure by altering the Additive Manufacturing (AM) process parameters, high process flexibility, high material utilization, a short production time, high repeatability and dimensional accuracy (Mostafaei, Amir et al. (2022)) and a material-

* Corresponding author.
E-mail address: sai_sreenivas.penkulinti@ensam.eu

10.1016/j.prostr.2024.03.089

saving technology because of the potential recycling of the raw material (e.g. reuse of unmelted metal powder in Powder bed fusion AM techniques). But limitations, like the presence of defects induced by the fabrication process, continue to be a crucial issue for the design of industrial components regarding fatigue damage, mainly Lack of Fusion (LoF) defects known for their tortuous morphology significantly reduce fatigue strength (DebRoy, T. et al. (2018), Kouraytem, Nadia et al. (June 2019), Sames, W. J. et al. (2016)).

Fatigue behaviour is sensitive to various parameters of the defect population (Murakami, Y (2002), El Khoukhi, Driss et al. (2021)), namely, size, morphology and spatial distribution (surface, sub-surface and internal) (Pablo, W et al. (2023)) and it is commonly admitted that defect size principally drives the fatigue strength in the uniaxial HCF regime (Ben Sghaier, R. et al. (2007) and Koutiri, I et al. (2013)). To define a defect size, the geometrical parameter $\sqrt{area}$ where the area is the projected area normal to the direction of maximum principal stress proposed by Murakami, Y. and Endo, M (1983) is widely used. However, this geometrical parameter is inapt to appropriately account for the criticality of complex morphology defects (LoF for e.g.) (Liu, Q.C et al. (2014)). Depending on the defect geometry and loading direction this $\sqrt{area}$ parameter may not fully capture the criticality of the defect. In addition, at times the effect of defect size ($\sqrt{area}$) is the same in tension and torsion (Billaudeau, T et al. (2004)) and it's not true all the time (Viet-Duc, L et al. (2016)).

In the HCF regime, for most of the alloys due to the strong influence of environmental factors on fatigue crack propagation, surface/sub-surface defects are more detrimental to fatigue behaviour compared to internal defects (Serrano-Munoz, Itziar et al. (2017), El Khoukhi, Driss et al. (2019)). Many studies (Wang, Q G et al. (2006), Koutiri, I et al. (2018), Buffière, J Y et al. (2001) Yadollahi, A et al. (2017) Mower, T M et al. (2016) Yamashita, Y et al. (2018)) have shown that even if a surface defect is 10 times smaller than an internal defect, a surface defect is detrimental to fatigue behaviour compared to an internal defect. In addition to the environmental effect, near-surface defects have different stress distributions due to free surface effects (Borbély, A et al. (2002)) which might promote crack initiation on surface or sub-surface defects instead of internal ones. Furthermore, in the work of Xu, Z et al. (2012), from elastoplastic simulations on an ideal defect, it was found that the stress concentration K_t was maximum when the whole spherical defect is in contact with the surface of the specimen.

It was observed that in cast AlSi alloy local defect morphology (defect's local geometrical imperfection) did not influence the fatigue strength (Rotella, Antonio et al. (2020)), but on the contrary, in Léopold, G. et al. (2015)'s work on cast Ti64 alloy (a high-strength material) the local defect morphology was the critical parameter for the fatigue strength. These results suggest a high impact of defect morphology on high-strength material as compared to ductile ones.

Studies on the impact of defects on multiaxial fatigue behaviour are limited, in particular, AM defects that are known for their complex morphology. In this study, using Finite Element (FE) simulations, in the particular case of multiaxial loading conditions, the key question that has been addressed is the impact of defects' morphology (LoF, gas pores) on the defect criticality (Guerchais, R et al. (2017)) and it is aimed to predict fatigue strength with respect to crack initiation only.

Nomenclature

E	Young's Modulus
ν	Poisson's ratio
K_t	Stress concentration
$\sigma_{d_{-1}}$	tensile fatigue strength at $R = -1$
$\tau_{d_{-1}}$	torsional fatigue strength at $R = -1$
σ_a	tensile stress amplitude at $R = -1$
τ_a	shear stress amplitude at $R = -1$
σ_{cr}	Crossland equivalent stress
$J_{2,a}$	2^{nd} invariant of deviatoric stress amplitude
$J_{1,max}$	Maximum hydrostatic stress
α & β	Crossland Criterion parameters
FIP	Fatigue Indicator Parameter

CD	Danger coefficient
Ψ	Sphericity

2. Material and Methods

The alloy considered in this study is Ti64, processed by L-PBF. The fatigue strengths a) $\sigma_{d_{-1}} = 512\ MPa$ (tensile fatigue strength at $R = -1$) and b) $\tau_{d_{-1}} = 416\ MPa$ (torsional fatigue strength at $R = -1$) have been obtained from samples that were stress relieved and Hot Isostatic Pressed (HIP) to significantly reduce residual stresses and porosity (experimental results from Vayssette, B et al. (2020)). In addition, experimental fatigue strengths for different defect populations have been obtained (this experimental work is not detailed in the present paper) and the main results are summarized in table 1.

Type of defects	defect size $\sqrt{area}\ \mu m$	$\sigma_{d_{-1}}$ MPa
Gas Pores	60	280
LoF	400	80

Table 1: Experimental results for specimens containing defects at surface loaded in tension at $R = -1$

2.1. Numerical procedure

Firstly, in the initial step, an ideal spherical defect generated numerically is placed at the centre of a cube and then subjected to meshing. The diameter of the spherical defect is one-fifth the length of the cube, and linear hexahedron elements are used for the meshing process. This configuration will be compared to simulations involving real defect geometries to evaluate the impact of the defect shape on fatigue strength. Three real defect geometries obtained from micro-CT scans (1) are meshed, and positioned at the centre of the cube, followed by meshing. For the aforementioned

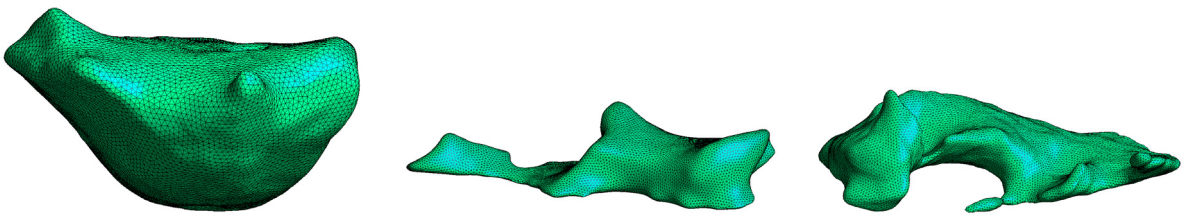

(a) (b) (c)

Fig. 1: Real defect geometries from micro-CT scans (a) defect 1, (b) defect 2 and (c) defect 3.

defects, the model is meshed using tetragonal linear elements. To accurately capture the stress and strain distributions surrounding the defects, a fine element size is controlled in the vicinity of the defects, 10 μm for an ideal spherical defect and 6.5 μm for defects 1, 2 and 3. One can note a difference in shape between defect 1 on one hand, and defects 2 and 3 on the other hand. This difference is reflected in sphericity (equation 1, where V_p is the volume of the defect and A_p is the surface area), the latter being 0.8 for defect 1, 0.5 for defects 2 and 3.

$$\Psi = \frac{\pi^{\frac{1}{3}} \left(6V_p\right)^{\frac{2}{3}}}{A_p} \tag{1}$$

For simulations in this present study, its behaviour is assumed to be linear elastic isotropic with Young's modulus $E = 110\ GPa$ and Poisson's ratio $\nu = 0.34$, and Multi-point Constraint (MPC) periodic boundary conditions are applied to impose three different loading conditions at a load ratio of $R = -1$. These loading conditions include

a) pure tension (σ_a), b) pure shear (τ_a), and c) in-phase combined tension-shear stress with a biaxial stress ratio of $\tau_a/\sigma_a = 1$. As the simulations are in elasticity, calculations are carried out by applying an arbitrary load of 100 MPa. In the post-processing step, depending upon the obtained stress values they are multiplied by the scaling factor to reach the threshold β which is discussed in the next subsection 2.2. Finite element calculations are performed using the FE code Z-set, while *GMSH* (Geuzaine, C et al. (2009)) is employed for the mesh generation of the models.

2.2. Multiaxial Fatigue Criterion

For ease of implementation in the FE tools, the Crossland criterion (Crossland, A. (1956)) is used for the fatigue behaviour prediction and is given by equation 2, where the Crossland equivalent stress σ_{cr} is a linear combination of the amplitude of the 2^{nd} invariant of deviatoric stress tensor $J_{2,a}$ and maximum hydrostatic stress $J_{1,max}$. The main hypothesis of this criterion is, it's valid for proportional loadings as most fatigue criteria in general.

$$\sigma_{cr} = \sqrt{J_{2,a}} + \alpha \cdot J_{1,max} \leq \beta \tag{2}$$

The calculation of $J_{2,a}$ (3) is obtained by the double maximisation over a loading period (Ben Sghaier, R. et al. (2007)). Where $\overline{\overline{S}}$ is the deviatoric stress tensor, $J_{1,max}$ is given by equation 4 and α and β parameters are identified from two fatigue strengths $\sigma_{d_{-1}}$ and $\tau_{d_{-1}}$ (Vayssette, B et al. (2020)).

$$\sqrt{J_{2,a}} = \frac{1}{2\sqrt{2}} max_{t_i \in T} \left\{ max_{t_j \in T} \sqrt{(\overline{\overline{S}}(t_i) - \overline{\overline{S}}(t_j)) : (\overline{\overline{S}}(t_i) - \overline{\overline{S}}(t_j))} \right\} \tag{3}$$

$$J_{1,max} = \frac{1}{3} max_{t_i \in T} \left\{ \sigma_{11}(t) + \sigma_{22}(t) + \sigma_{33}(t) \right\} \tag{4}$$

In the post-processing step, stress distributions on the surface of the defects are analysed by considering $\sqrt{J_{2,a}}$ and $J_{1,max}$ (or $\Sigma_{h,max}$) stress values which are used to plot a Crossland diagram as shown in figure 2. In the present case, Crossland equivalent stress σ_{cr} is the Fatigue Indicator Parameter (FIP) and fatigue strength is reached when the maximum FIP value on the surface of a defect (FIP_{max}), which is at point A on the figure 2, reaches the threshold β, or in other words if the danger coefficient $CD = \frac{FIP_{max}}{\beta}$ reaches a value of 1.

It has to be noted that in the current study stress gradients are not taken into account in the Criterion (local approach), and the model doesn't capture the effect of defect size on the criticality.

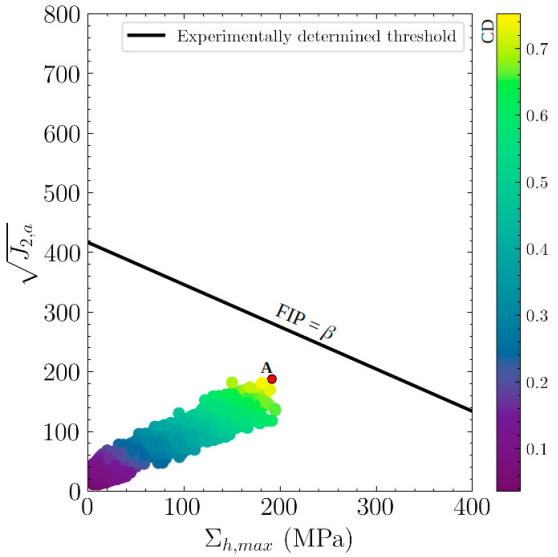

Fig. 2: Stress distributions on the surface of a defect represented in a Crossland diagram. Point **A** illustrates the maximum FIP value.

3. Results and Discussion

3.1. Macroscopic fatigue strengths determination

For all considered defects the macroscopic loads corresponding to the fatigue strengths are determined numerically. To do so, for a given defect, the macroscopic loading that has to be applied to have FIP_{max} equals to β can be directly assessed after the first calculation, as all calculations correspond to a linear problem (as mentioned in subsection 2.1). The identified macroscopic loads will be referred to as "macroscopic fatigue strength". For each defect and loading type, the $\sqrt{J_{2,a}}$ and $J_{1,max}$ values associated with the obtained macroscopic load are represented in the Crossland diagram as shown in figure 3. Firstly, a clear trend line can be noticed for the ideal spherical defect's numerical macroscopic stress values and a scatter in defects 1, 2 and 3 stress values. When the aforementioned trend line is compared with the experimental threshold line obtained from defect-free samples (from figure 2), there is a change in Crossland criterion parameters α (0.77 to 0.4) and β (416 to 171). This decrease in the α parameter in the presence of defects indicates a reduced sensitivity of the fatigue behaviour to the spherical part of the macroscopic stress tensor.

When the ideal spherical defect's numerical result is compared with the gas pore experimental fatigue strength, one can notice that the macroscopic fatigue strength determined numerically is underestimated, most likely due to the local approach which doesn't account for the high-stress gradients in the vicinity of the defects. The use of a non-local approach, for example by averaging σ_{cr} at each Gauss point over a determined characteristic volume V_c, would result in lower FIP and therefore higher macroscopic fatigue strength. However, it's worth pointing out: (a) the gas pores' (from experiments) morphology is not exactly the same as an ideal spherical defect (b) surface gas pores led to fatigue failure, whereas, in simulations, the defect is placed in the centre (internal defect case). These two aforementioned factors should also be accounted for to properly calibrate any non-local criterion.

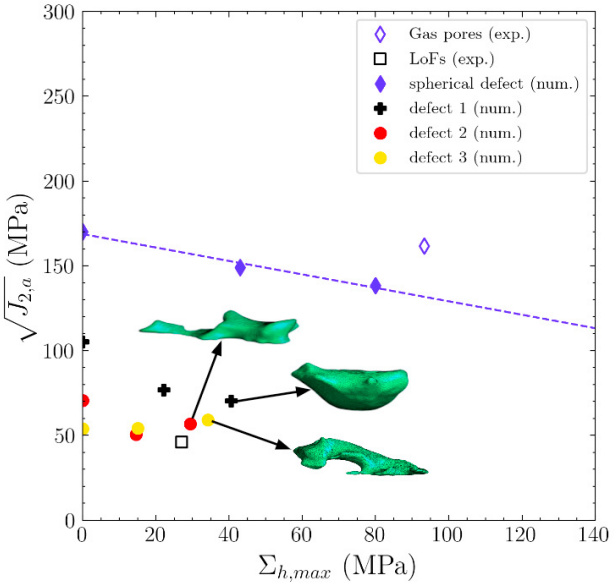

Fig. 3: Comparison of macroscopic numerical fatigue strengths with experimental ones for an ideal spherical defect and real defects from micro-CT scans loaded under pure tension, pure shear and combined tension-shear.

Secondly, when real defects' (defects 1, 2 and 3) numerical results are compared with the ideal spherical defect, a significant difference is observed. This difference is attributed to the high-stress concentrations induced by the tortuous shape of defects 1, 2 and 3, resulting in much lower macroscopic fatigue strength in comparison to an ideal spherical defect. To a lesser extent, one can also observe the difference between defect 1 which has a high sphericity value (0.8) and defects 2 and 3 whose sphericity values are 0.5. This confirms that the fatigue strength is sensitive to defect morphology. However, it should be noted that only a local fatigue criterion has been considered, which means that just one FIP value at the hot spot has been considered for fatigue strength prediction. If FIP values were averaged over

a characteristic volume V_c to account for the effect of stress gradients (refer subsection 2.5.3 in Vayssette, B et al. (2019)), local defect morphology would be expected to have less impact on the fatigue strength.

Comparing defects 1, 2 and 3's numerical fatigue strengths with the LoF defects' experimental fatigue strength, it can be observed that the numerical fatigue strengths are overestimated. This might be due to not taking into account the position of defects and also not considering the critical defect that led to fatigue failure. Indeed, the defect geometries considered in this study were chosen arbitrarily from the CT scan data and do not correspond necessarily to the most critical defect of the population. More calculations are required to find out if a criterion can be determined at a macroscopic scale, similar to the one determined for the ideal spherical defect.

Figure 4 illustrates the stress distributions on the surface of defects represented in a Crossland diagram. One can notice that even in the case of pure shear loading condition (figure 4 b, e and h) at a macroscopic scale, there are high hydrostatic stresses ($J_{1,max}$) in the vicinity of the defect. These results indicate that the presence of defect promotes high local hydrostatic stresses regardless of the macroscopic applied loading. This assumption is consistent with the decrease in α Crossland parameter observed for the defective material as compared with the defect-free material.

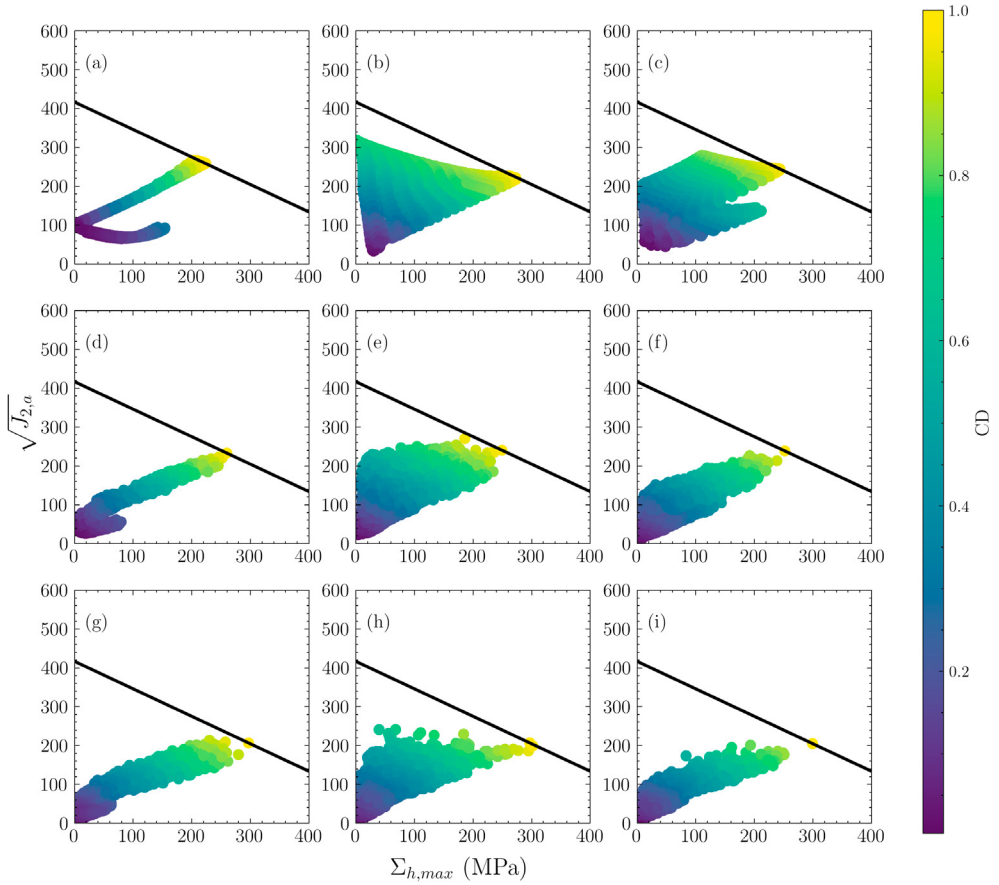

Fig. 4: Stress distributions on the surface of the defect: ideal spherical defect loaded under (a) tension, (b) shear and (c) combined tension-shear; defect 1 loaded under (d) tension, (e) shear and (f) combined tension-shear; defect 2 loaded under (g) tension, (h) shear and (i) combined tension-shear

3.2. Impact of defect geometry on the stress distribution

The FIPs on the surface of the defects are identified and when it's comprehended in terms of stress localization on the surface of the defect, as observed from the figure 5 localization of hot spots looks similar between the sphere and real defect geometries in tension case and it's no longer true for complex loading conditions. In the case of an

ideal defect hot spots or localization of the defect critical area is driven by the loading type and on the contrary defect 1 and 2's localization of the defect critical area is dominated by its morphology (hot spots on the region of highest curvature) and the same observation is made for defect 3. This shows that for complex shape defects, morphology is the principal parameter for localization of the defect critical area.

It is also important to note that real defect geometries obtained from micro-CT scans can have the same sphericity but different morphology, and sphericity should not be considered as the sole shape descriptor to analyse the fatigue behaviour, local shape descriptors (curvature for e.g.) might be taken into account. It is interesting to note that regardless of the loading type, the decrease in the sphericity tends to reduce the areas with high-stress concentrations.

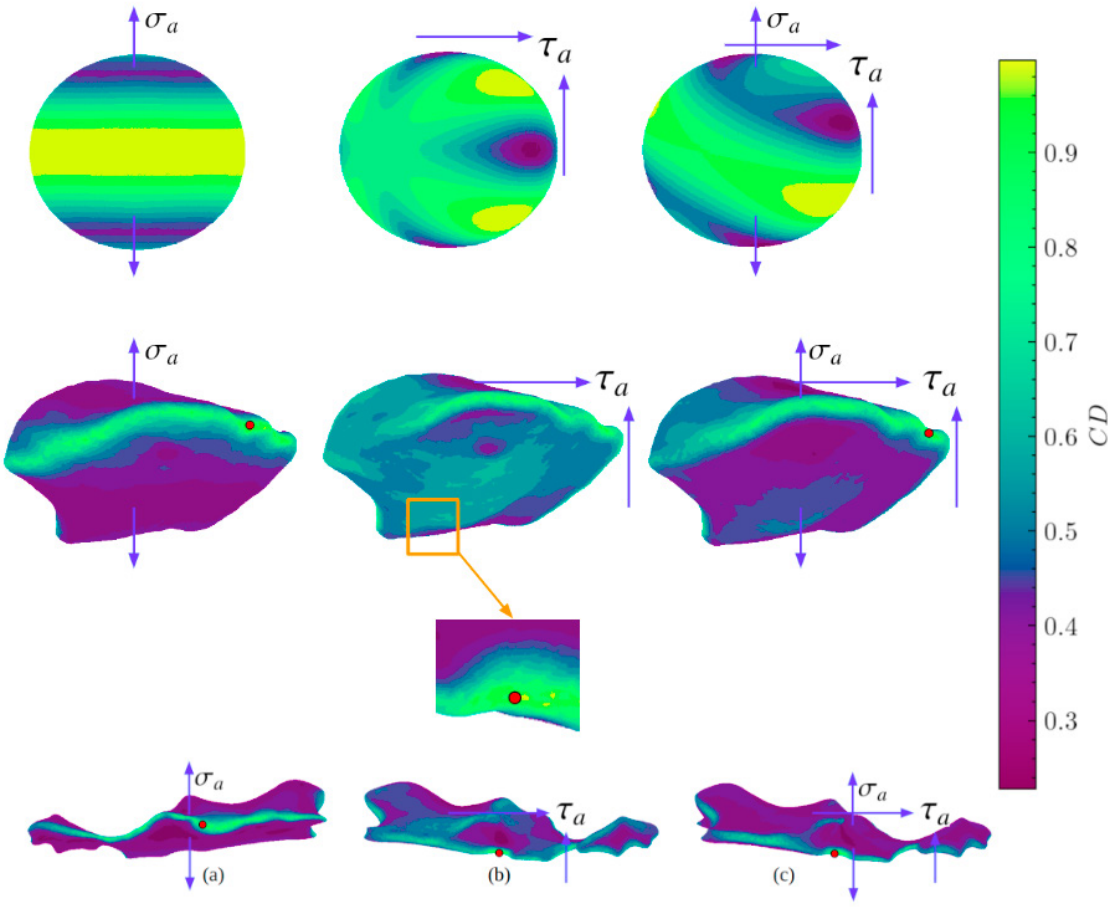

Fig. 5: Stress localization on the surface of an ideal defect, on defect 1 ($\Psi = 0.8$) and defect 2 ($\Psi = 0.5$) loaded under (a) pure tension, (b) pure shear and (c) combined tension-shear. Red dots on the surface of defects 1 and 2 indicate FIP_{max}.

4. Conclusions

In this work, from FE simulations under multiaxial loading conditions, in the presence of an ideal spherical defect and real defect geometries from micro-CT scans, the following conclusions can be drawn:

- In the presence of defects, the fatigue strength is less sensitive to the spherical part of the macroscopic stress tensor compared to the defect-free material.

- The underestimation of the fatigue strength for gas pores suggests that it's necessary to use a non-local fatigue criterion to properly predict the fatigue strength.
- Regardless of the loading type, the decrease in the sphericity tends to reduce the areas with high-stress concentrations.

Numerical work could be extended by accounting for the elastoplastic behaviour of the material and using a non-local approach to study the impact of stress gradient, by which the influence of defect size could be captured too.

Acknowledgements

References

Mostafaei, Amir et al., 2022. Defects and anomalies in powder bed fusion metal additive manufacturing. In: Current Opinion in Solid State and Materials Science 26.2, p. 100974. issn: 1359-0286. doi:https://doi.org/10.1016/j.cossms.2021.100974. url: https://www.sciencedirect.com/science/article/pii/S1359028621000772.

Pablo Wilson, Nicolas Saintier, Thierry Palin-Luc, Bruno Sudret, Sebastien Bergamo (2023). Statistical study of the size and spatial distribution of defects in a cast aluminium alloy for the low fatigue life assessment. International Journal of Fatigue, ff10.1016/j.ijfatigue.2022.107206ff.

Driss El Khoukhi, Franck Morel, Nicolas Saintier, Daniel Bellett, Pierre Osmond, Viet-Duc Le, Probabilistic modeling of the size effect and scatter in High Cycle Fatigue using a Monte-Carlo approach: Role of the defect population in cast aluminum alloys, International Journal of Fatigue, https://doi.org/10.1016/j.ijfatigue.2021.106177.

DebRoy, T. et al., 2018. In: Progress in Materials Science 92, pp. 112–224. ISSN: 0079-6425. URL: https://www.sciencedirect.com/science/article/pii/S0079642517301172.

Kouraytem, Nadia et al., June 2019. In: Phys. Rev. Appl. 11 (6), p. 064054. doi: 10. 1103 /PhysRevApplied.11.064054. url: https://link.aps.org/doi/10.1103/PhysRevApplied.11.064054.

Sames, W. J. et al., 2016. In: International Materials Reviews 61.5, pp. 315–360. doi 10.1080/09506608. 2015.1116649.

Viet-Duc Le, Franck Morel, Daniel Bellett, Nicolas Saintier, Pierre Osmond, Simulation of the Kitagawa-Takahashi diagram using a probabilistic approach for cast Al-Si alloys under different multiaxial loads, In: International Journal of Fatigue, https://doi.org/10.1016/j.ijfatigue.2016.08.014.

Y. Murakami, Metal Fatigue: Effects of Small Defects and Nonmetallic Inclusions, Elsevier.

Murakami, Y. and Endo, M 1983. In: Eng. Fract. Mech.

Murakami, Y. and Endo, M. 1986. In: The Behaviour of Short Fatigue Cracks, (Ed. K.J. Miller and E.R. de los Rios), EGF Publication 1, Mechanical Engineering Publications, London.

Serrano-Munoz, Itziar et al. (2017). "Location, location & size: Defects close to surfaces dominate fatigue crack initiation". In: Scientific Reports 7. doi:10.1038/srep45239.

El Khoukhi, Driss et al. (2019). "Experimental investigation of the size effect in high cycle fatigue: Role of the defect population in cast aluminium alloys". In: International Journal of Fatigue 129, p. 105222. issn: 0142-1123. doi:https://doi.org/10.1016/j. ijfatigue.2019.105222.

Rotella, Antonio et al. (2020). "Influence of defect morphology and position on the fatigue limit of cast Al alloy: 3D characterization by X-ray microtomography of natural and artificial defects". In: Materials Science and Engineering: A 785, p. 139347. issn: 0921-5093. doi:https://doi.org/10.1016/j.msea.2020.139347.

Léopold, G. et al. (2015). "Influence of artificial and casting defects on fatigue strength of moulded components in Ti6Al4V alloy". In: Fatigue & Fracture of Engineering Materials & Structures 38.9, pp. 1026–1041. doi: https://doi.org/10.1111/ffe.12326.

Ben Ahmed, A., A. Nasr, A. Bahloul, and R. Fathallah. (2017). "The Impact of Defect Morphology, Defect Size, and SDAS on the HCF Response of A356-T6 Alloy." The International Journal of Advanced Manufacturing Technology 92 (1): 1113–25. https://doi.org/10.1007/s00170-017-0192-6.

Koutiri, Imade, Daniel Bellett, Franck Morel, Louis Augustins, and Jérôme Adrien. (2013). "High Cycle Fatigue Damage Mechanisms in Cast Aluminium Subject to Complex Loads." International Journal of Fatigue 47 (February): 44–57. https://doi.org/10.1016/j.ijfatigue.2012.07.008.

Bastien Vayssette, Nicolas Saintier, Charles Brugger, Mohamed El May. (2020). Surface roughness effect of SLM and EBM Ti-6Al-4V on multiaxial high cycle fatigue. In: Theoretical and Applied Fracture Mechanics, https://doi.org/10.1016/j.tafmec.2020.102581.

Geuzaine, C and J.F. Remacle, J F. (2009). Gmsh: a three-dimensional finite element mesh generator with built-in pre and post-processing facilities. In: International Journal for Numerical Methods in Engineering.

Crossland, A. (1956). "Effect of large hydrostatic pressures on the torsional fatigue strength of fan alloy steel". In: Proceedings of the international conference on fatigue of metals.

Ben Sghaier, R. et al. (2007). In: International Journal of Fatigue 29.2, pp. 209–221. Issn: 0142-1123. doi https://doi.org/10.1016/j.ijfatigue.2006.03.015.

R. Guerchais, F. Morel, N. Saintier (2017), Effect of defect size and shape on the high-cycle fatigue behavior, International Journal of Fatigue, https://doi.org/10.1016/j.ijfatigue.2016.12.010.

Borbély, A., Mughrabi, H., Eisenmeier, G. et al. A finite element modelling study of strain localization in the vicinity of near-surface cavities as a cause of subsurface fatigue crack initiation. International Journal of Fracture 115, 227–232 (2002). https://doi.org/10.1023/A:1016350528652

Bastien Vayssette, Nicolas Saintier, Charles Brugger, Mohamed El May, Etienne Pessard. (2019). Numerical modelling of surface roughness effect on the fatigue behavior of Ti-6Al-4V obtained by additive manufacturing, In: International Journal of Fatigue, https://doi.org/10.1016/j.ijfatigue.2019.02.014

M. Vincent, Y. Nadot, C. Nadot-Martin, A. Dragon 2016, Interaction between a surface defect and grain size under high cycle fatigue loading: Experimental approach for Armco iron, International Journal of Fatigue, https://doi.org/10.1016/j.ijfatigue.2016.01.013

Liu, Q.C., Elambasseril, J., Sun, S.J., Leary, M., Brandt, M., Sharp, P.K., 2014. The Effect of Manufacturing Defects on the Fatigue Behaviour of Ti-6Al-4V Specimens Fabricated Using Selective Laser Melting. AMR 891–892, 1519–1524. https://doi.org/10.4028/www.scientific.net/amr.891-892.1519

T. Billaudeau, Y. Nadot, G. Bezine, Multiaxial fatigue limit for defective materials: mechanisms and experiments, Acta Materialia, Volume 52, Issue 13, https://doi.org/10.1016/j.actamat.2004.05.006

Wang QG, Crepeau PN, Davidson CJ, Griffiths JR (2006). Oxide films, pores and the fatigue lives of cast aluminium alloys.

Koutiri I, Pessard E, Peyre P, Amlou O, De Terris T (2018). Influence of SLM process parameters on the surface finish, porosity rate and fatigue behaviour of as-built Inconel 625 parts. J Mater Process Technology.

Buffière J Y, Savelli S, Jouneau PH, Maire E, Foug‘eres R (2001). Experimental study of porosity and its relation to fatigue mechanisms of model Al–Si7–Mg0.3 cast Al alloys. Mater Sci Engng, A.

Yadollahi A, Shamsaei N, Thompson SM, Elwany A, Bian L (2017). Effects of building orientation and heat treatment on fatigue behaviour of selective laser melted 17-4 PH stainless steel. Int J Fatigue.

Mower TM, Long MJ (2016). Mechanical behaviour of additively manufactured, powder-bed laser-fused materials. Mater Sci Engng, A.

Yamashita Y, Murakami T, Mihara R, Okada M, Murakami Y (2018). Defect analysis and fatigue design basis for Ni-based superalloy 718 manufactured by selective laser melting. Int J Fatigue.

Xu, Z., Wen, W. & Zhai, T (2012). Effects of Pore Position in Depth on Stress/Strain Concentration and Fatigue Crack Initiation. https://doi.org/10.1007/s11661-011-0947-x